Math. Model. Nat. Phenom. 21 (2026) 15
https://doi.org/10.1051/mmnp/2025028

Mathematical Modelling of Natural Phenomena
www.mmnp-journal.org

IN SILICO PHASE-FIELD MODELING OF CELL DIRECTED MIGRATION TOWARDS ENVIRONMENTS OF LOWER OR HIGHER ADHESION

Lucas Curci[1], Valentine Seveau de Noray[2], Olivier Theodoly[2], Marie-Pierre Valignat[2], Florence Hubert[1] and Julien Olivier[1,*]

Abstract. This work focuses on modeling adhesive haptotaxis in cell migration. While cells typically move toward regions of high adhesiveness, experiments on lymphocytes at the Laboratory of Adhesion & Inflammation (LAI) in Marseille have revealed an opposite behavior known as reverse adhesive haptotaxis. To investigate this phenomenon, we adapt a single-cell migration model originally proposed by Aronson and Ziebert [*Soft Matter* **10** (2014) 1365–1373, *PLoS One* **8** (2013) 1–14, *J. Roy. Soc. Interface* **9** (2012) 1084–1092], which accounts for the dynamics of adhesion site density. In our adaptation, we exclude contractility and rear adhesion—factors likely irrelevant for lymphocyte propulsion [Aoun *et al.*, *Biophys. J.* **119** (2020) 1157–1177] – and explore the role of adhesion signaling in two key processes: (i) propulsion at the cell front, as previously proposed in Ziebert and Aranson [*PLoS One* **8** (2013) 1–14], and (ii) actin polymerization within the cell, a novel aspect of this study. By thoroughly analyzing the interplay between these mechanisms, we demonstrate that our model can capture both classical and reverse haptotaxis. Notably, reverse haptotaxis emerges in this context when propulsion is coupled with positive feedback signaling mechanism but also when actin polymerization is coupled with negative feedback mechanism, suggesting the need for future experimental efforts to identify the corresponding signaling cascade in lymphocytes.

Mathematics Subject Classification. 35Q92, 92C37, 65M08.

Received August 3, 2024. Accepted October 24, 2025.

1. Introduction

Cell migration, the process by which cells move from one location to another is crucial in a myriad of living processes, like food search, reproduction, growth, infection and immune response. The migration of nucleated cells (eukaryotic cells), among which human cells, results from the coordinated interplay of adhesion of the cell surface to the environement coupled to growth and contraction of an inner cytoskeleton that deform cells shape. Adhesion is notably mediated by specialized proteins of the integrins family, which connect the cell's cytoskeleton to the extracellular matrix, enabling traction and movement. Growth or protrusion results from polymerization of the actin protein at the leading edge that pushes the membrane forward and form lamellipodia and filopodia.

Keywords and phrases: Haptotaxis, adhesion, directed cell migration, phase field models.

[1] Aix Marseille Univ, CNRS, I2M, Turing Centre for Living systems, Marseille, France.
[2] Aix Marseille Univ, CNRS, INSERM, LAI, Turing centre for living systems, Marseille, France.

* Corresponding author: julien.olivier@univ-amu.fr

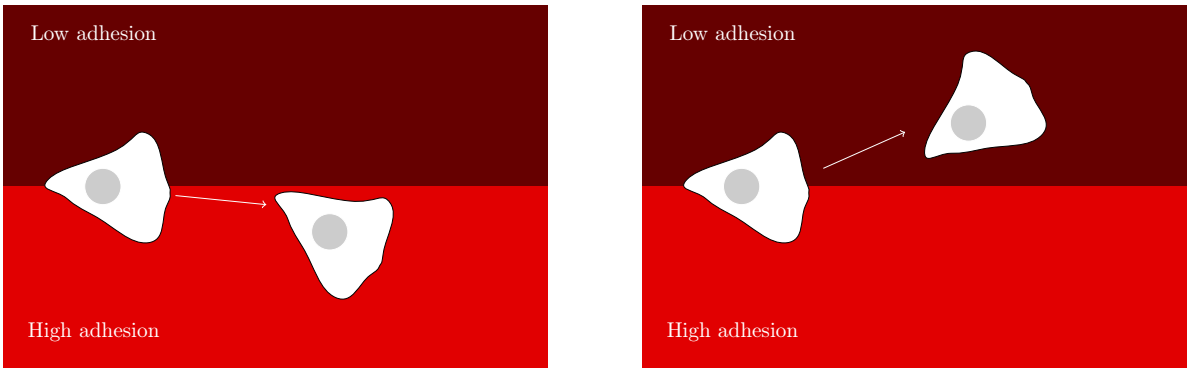

(A) Classical adhesive haptotaxis (B) Reverse adhesive haptotaxis

FIGURE 1. Diagram of adhesive haptotaxis and reverse adhesive haptotaxis.

This allows a cell to explore the environment and initiate new contacts with the substrate. Simultaneously, contractile forces in the cell cytoskeleton are mediated by the motor proteins myosin II, that arguably allow a cell to maintain membrane tension, detach its rear, and participate to the backwards treadmilling of the cytoskeleton.

Mesenchymal cells, including cancer cells, fibroblasts, endothelial cells, and neurons, develop strong pulling forces with their substrates. Mesenchymal migration requires firm adhesion provided by the maturation of nascent adhesions at cell leading edges into mature anchoring focal adhesions. Mesenchymal cells are known to be guided by modulations of the adhesion properties of their environment, with a systematic bias towards more adhesive zones. We call for convenience this phenomenon classical adhesive haptotaxis (see Fig. 1a). A "tug of war" competition between the cell's adherent edges may determine a mechanical drift motion towards areas with higher adhesion by compliance of cells edges anchored on less adherent zones [1]. Another point of view considers that integrins may send a biological signal when engaged with their ligand that may stimulate actin polymerization and lamellipodium growth rate. Cells would then reorient towards higher adhesive zones by a faster differential spreading of their leading edge on regions with higher ligand density [2]. Both mechanisms by a mechanical "tug of war" bias or a biosignaling guidance explain directed motion towards more adhesive regions.

A recent study by Luo *et al.* [3] revealed that guidance by adhesion was not limited to mesenchymal cells. Amoeboid cells, which includes leukocytes and some cancer cells, do not require adhesion to move and are not confined by adhesive area [4], in contrast to mesenchymal cells, but they are nevertheless guided by exquisite modulations of adhesion. Furthermore, using substrates coated with VCAM-1, a ligand of the integrin VLA-4, Luo *et al.* observed classical adhesive haptotaxis, with cells migrating toward areas of higher adhesion. In contrast, on substrates coated with ICAM-1, a ligand of the integrin LFA-1, they identified a counter-intuitive phenotype, where cells oriented toward lower adhesion zones (Figs. 1b and 2). Reverse haptotaxis directs cells toward regions where they increase their energy, which appears incompatible with passive physical mechanisms. Moreover, existing active biosignaling models from the literature [2] consistently predict standard haptotaxis toward higher adhesion zones. As a result, no current mechanism fully explains this unexpected behavior.

Here, we focus on modeling the haptotactic response of amoeboid cells, for which the essential elements of migration are adhesion and actin polymerization. Numerous mathematical models of cell migration exist in the literature, varying in their level of details. These models can simulate mechanisms such as cell adhesion to the substrate or the protrusion dynamics of the cell. Notably, the group of Aronson and Ziebert [5–7], were pioneers in using a phase-field method to represent the cell membrane in migration problems. We choose this approach as our starting point, neglecting the effects of contractility, which are not crucial for lymphocyte migration [8]. We use the Discrete Duality Finite Volumes (DDFV) discretization framework for this phase-field model, and

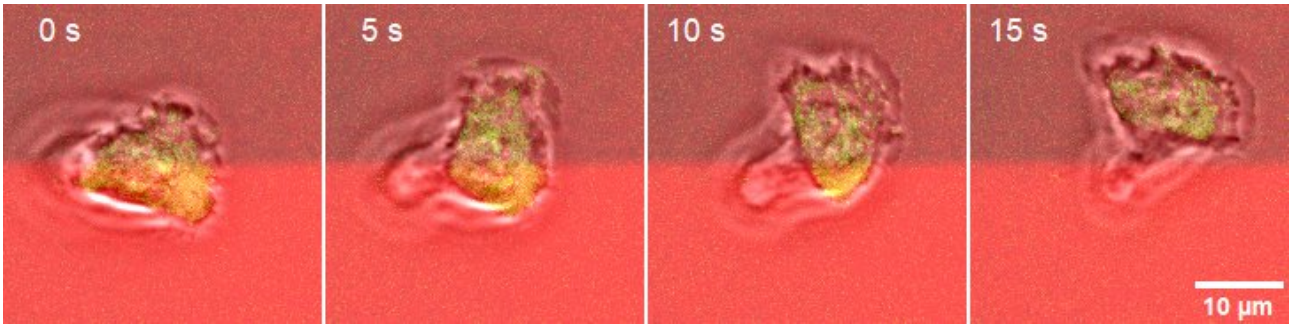

FIGURE 2. Lymphocytes performing reverse adhesive haptotaxis on a substrate consisting of adhesive bands corresponding to different densities of adhesion ligands (ICAM-1). Superposition of brightfield microscopy image showing the cell (grey), fluorescence microscopy image showing ICAM ligand density (brown for a low density and red for a high density), and interferometry microscopy image showing the adhesion footprint of the cell (green).

discuss how it is adapted in the context of cell migration. Our findings reveal that parameters such as propulsion and actin polymerization (see Sect. 2.1.1 for a mathematical description of these parameters) are critical factors in the dynamics of cell migration. Specifically, for cells at the frontier between two zones of different adhesion, we investigate how adhesion dynamics impact actin polymerization. To this end, we introduce a coupling term in the actin network orientation equation, influencing polymerization. This leads to the following finding: when this new coupling is activated and propulsion coupling is deactivated, simulations show migration towards areas of higher adhesion, indicating classical adhesive haptotaxis. Furthermore, when the propulsion coupling is activated, our in silico experiments demonstrate migration towards areas of lower adhesion. By simultaneously studying these two couplings, we could reproduce versatile haptotactic phenomena, whether classical or reverse.

In Section 2, we present first some phase-field models inherited from Aronson and Ziebert [6], then the modifications that we made in order to adapt it to lymphocyte migration and finally we present the DDFV discretisation of our model. In Section 3, we show simulations of the model that display both classical and reverse adhesive haptotaxis and then we study which one appears, as a function of the parameters of the model. In Section 4, we discuss limitations of this model and perspectives to consider additional aspects of haptotactic phenotypes such as the rebound of a cell against the sharp frontier of a zone with higher adhesion.

2. A PHASE-FIELD MODEL FOR ADHESIVE HAPTOTAXIS

2.1. The model

2.1.1. Previous models for keratocytes

The model we present in Section 2 is based on previous studies from the group of Ziebert and Aronson on the modeling of the migration of keratocytes on adhesive and elastic substrates. Their goal was to reproduce in silico several known modes of migration of these keratocytes and also the different shapes the keratocytes adopt during migration. Let us describe their model. It couples several equations, each taking into account the dynamics of different parts of the biological system.

The first one describes the position and shape of the cell through a variable ρ. In [7] and sequels, they have adopted what is known as a *phase-field* description. In short, the function ρ of time and space takes value 0 outside the cell and 1 inside the cell. In practice, ρ is allowed to vary smoothly in the mathematical sense but sharply enough so that it is sensible to consider that the cell occupies the domain $\{\rho \geq 1/4\}$. Note that in this framework, if the model is to be usable at any time t, ρ should have a certain structure: at "most" places ρ should be almost equal to 0 or almost equal to 1 and in between the value of ρ should vary rapidly on a length scale which can then be interpreted as a thickness of the membrane of the cell. This is important to bear in

mind because then $\nabla\rho$ is 0 "almost everywhere" except "in the membrane" in which it points from the outside of the cell to the cell. This is a fact that is used in the subsequent modelling.

The second quantity represented in this model is a vector field noted $\overrightarrow{p}$ which represents *the average orientation of the actin network* in a neighbourhood of a point. Let us recall that at the leading front of the cell, that is in lamellipodia and filopodia, where actin is highly polymerized, actin filaments are branched in parallel organization where actin polymerizes and forms a polarized active gel growing at the leading edge of the cell. At the opposite at the rear of the cell actin is branched into anti-parallel organization. This means that, locally, the vector $\overrightarrow{p}$ provides information on the orientation of the actin field, as well as the intensity of its polymerization : the larger $|\overrightarrow{p}|$, the more actin filaments are branched in a parallel pattern, and inversely if $|\overrightarrow{p}|$ is small, the actin filaments are branched in an anti-parallel pattern.

In [6], the dynamics of these two quantities is given by the following system:

$$\begin{aligned}\partial_t\rho &= D_\rho\Delta\rho - \rho(1-\rho)(\delta[\rho]-\rho) - \alpha\overrightarrow{p}\cdot(\nabla\rho)\\ \partial_t\overrightarrow{p} &= D_{\overrightarrow{p}}\Delta\overrightarrow{p} - \tau_1\overrightarrow{p} - \tau_{1,out}(1-\rho)^2\overrightarrow{p} - \beta(\nabla\rho) - \gamma[\overrightarrow{p}\cdot\nabla\rho]\overrightarrow{p}\end{aligned}$$

where

$$\delta[\rho](t,x,y) = \frac{1}{2} + \mu\left(\int\rho(t,x',y')\mathrm{d}x'\mathrm{d}y' - \int\rho(0,x',y')\mathrm{d}x'\mathrm{d}y'\right) - \sigma|\overrightarrow{p}(t,x,y)|^2. \tag{2.1}$$

The first equation is a modified Allen-Cahn equation. The standard Allen-Cahn equation is historically used to describe physical systems in two phases (like gas and liquid mixtures for instance). In our biological context the two phases would be "cell" and "not cell" so they are obviously not interacting in the same way as pure material. For instance, liquid bubbles can shrink and disappear as they are evaporated a behavior that the Allen-Cahn equation reproduces very well. On the contrary, cells remain of roughly the same size during migration (albeit in various shapes). So the first modification of the Allen-Cahn that has to be made is to include a mechanism to preserve cell size. It is done by using $\delta[\rho]$ wherein a classical Allen-Cahn equation we would have a constant term. To understand this mechanism, let us first put ourselves in this classical setting where we have a fixed constant δ_0 in place of $\delta[\rho]$. When $\delta_0 > 1/2$ the phase represented by the value $\rho = 0$ is, in a sense, favored and tends to invade and absorb the unfavored phase $\rho = 1$. In the biological context it means that the cell tends to shrink since the "not cell" phase invades the "cell" phase. The situation is reversed when $\delta_0 < 1/2$. Now imagine we have $\delta[\rho]$ but with $\sigma = 0$, in which case $\delta[\rho]$ depends only on time. Then if at time t the cell is "too large" (respectively "too small") then $\delta[\rho](t) > 1/2$ (respectively $\delta[\rho](t) < 1/2$) in which case the "not cell" is favored (respectively the "cell" is favored). The idea is to dynamically favor the right phase to compensate an unwanted growing or shrinking behavior. As can be seen in their numerical simulations or ours, it turns out that this mechanism is quite efficient at fulfilling its role. The term $-\sigma|\overrightarrow{p}|^2$ is a way to model the effect of contractility on the control of the size and the shape of the cell.

Moreover, the Allen-Cahn equation is designed to modify ρ based on what is called *mean curvature* motion of the interface which, while relevant in the biological context, is not sufficient to describe accurately the interaction of the cell with its environment. The second modification that they have made is thus adding a drift term to the equation with a transport velocity proportional to the mean orientation of the actin network $\overrightarrow{p}$ (with a constant of proportionality α) to take into account the effect of polymerization on the motion of the cell.

The second equation is a reaction-diffusion equation describing the evolution of the variable $\overrightarrow{p}$. It consists in a diffusion term $D_p\Delta\overrightarrow{p}$, a term accounting for actin depolymerization $-\tau_1\overrightarrow{p}$, an active term $\beta\nabla\rho$ accounting for the effects of creation of actin due to polymerization. The $-\gamma[\overrightarrow{p}\cdot\nabla\rho]\overrightarrow{p}$ term models the action of myosin motors, which are very present at the rear of the cell, degrading the mean orientation of actin network $\overrightarrow{p}$ by assembling actin filaments in an anti-parallel organization (contractile bundles) to create stress fibers. The last term $-\tau_{1,out}(1-\rho)^2\overrightarrow{p}$ is there to artificially attenuate $\overrightarrow{p}$ outside the cell, strongly enough to eliminate it rapidly. With phase-field methods, since biological material is not transported with the cell, and thus could remain while the cell has moved, we have to use this "trick" to eliminate this non-biological effect.

After this initial model, the group of Aronson and Ziebert added the interaction of the cell with the adhesive elastic substrate in [5, 6]. They did so by introducing a scalar field noted A_{dh} which describes the density of adhesion links forming between the cell and the extracellular matrix.

Then the interaction between the cell and the substrate is basically twofold: first the density of links between the cell and the substrate influence the motion of the cell and the polymerization activity; second links are created and broken dynamically depending on the mechanical properties of the substrate. The first point translates mathematically in the fact that the formerly constant α will now become a function of the level of adhesion A_{dh}. The second point is taken into account into a new reaction-diffusion equation on A_{dh} to describe its dynamics:

$$\partial_t A_{dh} = D_A \Delta A_{dh} + \rho \left(a_0 |\overrightarrow{p}|^2 + a_{nl} A_{dh}^2 \right) - s A_{dh}^3 - d(U) A_{dh}$$

In this equation a_{nl} and s are constants characterizing, among other parameters, the adhesive properties of the substrate, and more specifically the easiness for the cell to reinforce existing links or to unbind them. The coefficient a_0 depends on the local adhesive properties of the substrate and describes the ability for the cell to form bonds where polymerization occur. This creation term is proportional to $|\overrightarrow{p}|^2$. This means that adhesion links will be created at the front of the cell (in the direction of its movement), *i.e.*, in the area where actin is highly polymerized. In this sense, the variable $|\overrightarrow{p}|^2$ also plays a signaling role between the front and the back of the cell. Finally $d(U)$ is a coefficient linked to the local deformation of the substrate and takes into account the links that are broken because of a too strong deformation of the substrate. This term is thus fundamentally linked to the elasticity of the substrate. One should then add an equation on the deformation of the substrate but we refer to [5, 6] for further details.

2.1.2. Our model for lymphocyte migration

In order to capture the specificity of adhesive haptotaxis performed by lymphocytes we adapt the model from [5, 6].

We have seen in the introduction that the contractility of the cell is a negligible effect for lymphocytes [4, 8]. Thus, we can neglect the two terms related to the contractility of the cell. The first of these terms is $-\sigma|\overrightarrow{p}|^2$, with $\sigma \geq 0$, in the volume conservation equation (2.1). Mainly this term acts on the shape of the cell, which gives "crescent-like" shape, typical of keratocytes, when σ is large, and a "fan-like" shape, more suitable to lymphocytes, when this parameter is set close to 0 (see [7] for these results). For this reason, we take $\sigma = 0$ in our model. The second of these terms is $-\gamma[\overrightarrow{p} \cdot \nabla\rho]\overrightarrow{p}$ modeling the contractility due to myosin motors. Consequently, we take $\gamma = 0$ in what follows.

We then modify substantially the equation governing the variable A_{dh} focusing on the haptotactic response of lymphocytes. Driven by the experiments which are conducted on non deformable extra-cellular matrices, we remove the dependency of the detachment term on the deformation. We also removed the non linear terms modeling collective and saturation effects of adhesion links $a_{nl}A_{dh}^2$ and sA_{dh}^3, which were more difficult to connect to biological factors, to keep only the creation and linear detachment of adhesion terms. We also add a term $a_{1,out}(1-\rho)^2 A_{\mathrm{dh}}$ to the equation (2.2c), which removes adhesion links outside the cell. This parallels the actin depolymerization term outside of the cell present in equation (2.2b).

The major originality of our work is to consider that the adhesion site density can modulate not only the propulsion term $\alpha(A_{\mathrm{dh}})\overrightarrow{p} \cdot \nabla\rho$ in equation (2.2a) but also the creation of actin due to the polymerization. Indeed, integrins are known to serve as mechanotransducers that link extracellular matrix adhesion to intracellular actin remodeling, playing a crucial role in cell migration and adhesion-dependent signaling. This process occurs through a series of intracellular signaling pathways that link integrin activation to the actin cytoskeleton. The cytoplasmic tails of integrins recruit focal adhesion proteins like talin and kindlin, which help link integrins to the actin cytoskeleton. Integrins further activate small GTPases such as Rac1 in lamellipodia that promote actin polymerization through the Arp2/3 complex. In our model, we accordingly added the coupling $\beta(A_{dh})\nabla\rho$

in equation (2.2b) and since adhesion generally promotes local actin polymerization, the coefficient β is *a priori* positive. Note that the latter coupling was not studied in [6] in which the term $\beta(A_{dh})$ is held constant.

Let Ω be bounded subset of $\mathbb{R}^2$. In practice, we only work with a rectangle. We end up with the system, for $t > 0$ and $x \in \Omega$:

$$\partial_t \rho = D_\rho \Delta \rho - \rho(1-\rho)(\delta[\rho] - \rho) - \alpha(A_{dh})\overrightarrow{p} \cdot (\nabla \rho) \tag{2.2a}$$

$$\partial_t \overrightarrow{p} = D_{\overrightarrow{p}} \Delta \overrightarrow{p} - \tau_1 \overrightarrow{p} - \tau_{1,out}(1-\rho)^2 \overrightarrow{p} - \beta(A_{dh}) \nabla \rho \tag{2.2b}$$

$$\partial_t A_{dh} = D_A \Delta A_{\mathrm{dh}} + \rho a_0(x,y) |\overrightarrow{p}|^2 - a_1(x,y) A_{dh} - a_{1,out}(1-\rho)^2 A_{dh} \tag{2.2c}$$

with, for $x \in \partial\Omega$, homogeneous Dirichlet boundary conditions:

$$\rho(t,x) = 0 \qquad \overrightarrow{p}(t,x) = \begin{pmatrix} 0 \\ 0 \end{pmatrix} \qquad A_{\mathrm{dh}}(t,x) = 0 \tag{2.3}$$

and initial conditions:

$$\rho(0,x) = \rho_0(x) \qquad \overrightarrow{p}(0,x) = \overrightarrow{p_0}(x) \qquad A_{\mathrm{dh}}(0,x) = 0 \tag{2.4}$$

We limit ourselves to functions α and β which are linear in A_{dh},

$$\alpha(A_{dh}) = \alpha_0 + \alpha_1 A_{dh}, \qquad \beta(A_{dh}) = \beta_0 + \beta_1 A_{dh}. \tag{2.5}$$

The adhesiveness properties of the substrate can be varied in space through two parameters: one contributing to detachment of adhesion links $a_1(x,y)$ and the other to creation of adhesion links $a_0(x,y)$. In equation (2.2c), the term for adhesion creation is proportional to a_0, which physically represents a combination of ligand density—affecting the statistical likelihood of bond formation—and the kinetic engagement constant k_{on} between integrins and their ligand. Adhesion creation is also chosen to be proportional to $|\overrightarrow{p}|^2$, although this lacks a direct physical meaning, as actin polymerization does not promote adhesion—rather, it tends to have the opposite effect. However, lymphocyte migration is characterized by a robust polarization machinery that enhances LFA-1 mediated adhesion at the front of the cell and inhibits it at the rear [9]. The inclusion of $|\overrightarrow{p}|^2$ allows for a polarization-dependent coupling in adhesion formation, as $\overrightarrow{p}$ is inherently polarized in our model. We focus here on adhesion bands or gradients generated by a variation of the detachment parameter a_1. The case of substrates generated by a variation of the creation parameter a_0 is shown in the Appendix and yield exactly similar trends as with a_1.

Table 1 summarizes the parameters involved in the system (2.2). These parameters are either new parameters, or parameters taken from [6].

2.2. Discretisation of the model in DDFV framework

We now discretize the system (2.2) using the DDFV formalism with the notations of [10]. This finite volume approach has been introduced in [11, 12] to approximate elliptic operators on general meshes. It has been then extended to a large variety of more complex problems: nonlinear elliptic problems in [10, 13], convection-diffusion problems [14] Stokes problems [15, 16], Navier Stokes problems [17], Peaceman model [18], Maxwell problems [19], level-set problems [20–22], hyperbolic problems [23], Cahn-Hilliard problems [24], ... In our case, to reduce the cost of computation, we use cartesian meshes locally refined in the neighborhood of the cell, making the use of DDFV approach relevant.

All the unknowns are approximated, at each time iteration $t_n = n\Delta t$, on both the primal ($\mathcal{M}$) and dual meshes ($\mathcal{M}^*$). For $\mathcal{T} = \mathcal{M} \cup \mathcal{M}^*$, we thus introduce $\rho^{\tau,n} = (\rho_C^n)_{C \in \mathcal{T}}$, $\overrightarrow{p}^{\tau,n} = (u_C^n, v_C^n)_{C \in \mathcal{T}}$, $A^{\tau,n} = (A_C^n)_{C \in \mathcal{T}}$.

We use the classical discrete DDFV gradient and divergence operator $\nabla^{\mathcal{D}}$ and $\mathrm{div}^{\mathcal{T}}$. We also require an interpolation $\nabla^{\mathcal{T}}$ of the classical discrete operator $\nabla^{\mathcal{D}}$ (himself defined on the diamond mesh) on the primal

TABLE 1. Table of parameters for Model (2.2). Reference values are given for all parameters. The range or set of values when parameters are varied is indicated in parentheses.

Param.	Value	
D_ρ	1	Diffusion of ρ
$D_{\overrightarrow{p}}$	0.2	Diffusion of $\overrightarrow{p}$
D_A	1	Diffusion of A_{dh}
κ	0.01	Parameter controlling the initial thickness of the cell
(x_0, y_0)	$(25, 50)$	Initial position of the cell's center of mass
r_0	15	Initial radius of the cell
τ_1	0.1	Depolymerization/degradation of $\overrightarrow{p}$ inside the cell
$\tau_{1,\mathrm{out}}$	0.4	Depolymerization/degradation of $\overrightarrow{p}$ outside the cell
$a_{1,\mathrm{out}}$	1	Detachment of adhesion sites outside the cell
a_0	0.025 (0–0.025)	Creation of adhesion sites
a_1	0.3 (0.1–0.3)	Detachment of adhesion sites inside the cell
α_0	3 $(2; 2.5; 3)$	Cell propulsion coefficient
β_0	1.5 $(1; 1.5; 2)$	Actin polymerization coefficient
α_1	30 $(-10; 30)$	Adhesion/propulsion coupling coefficient of the cell
β_1	30 $(-10; 60)$	Adhesion/actin polymerization coupling coefficient

and dual meshes, constructed as a natural projection of $\nabla^{\mathcal{D}}$ on the primal and dual cells. The consistency of this approach has been validated on manufactured test cases in [25] exhibiting a spatial convergence order equal to 2.

The discretization of the system of equations (2.2) is then obtained by a semi-implicit time discretization and DDFV in space for each equation in the system. For any $\mathrm{C} \in \mathcal{M} \cup \mathcal{M}^*$, we obtain:

$$\begin{aligned}
\frac{\rho_{\mathrm{C}}^{n+1} - \rho_{\mathrm{C}}^n}{\Delta t} &= D_\rho \left(\mathrm{div}^\tau \nabla^{\mathcal{D}} \rho^{\tau,n+1}\right)_{\mathrm{C}} - \rho_{\mathrm{C}}^n (1 - \rho_{\mathrm{C}}^n)(\delta[\rho^n] - \rho_{\mathrm{C}}^n) \\
&\quad - \alpha(A_{\mathrm{C}}^n) \overrightarrow{p}_{\mathrm{C}}^n \cdot (\nabla^\tau \rho^{\tau,n})_{\mathrm{C}} \qquad (2.6a) \\
\frac{u_{\mathrm{C}}^{n+1} - u_{\mathrm{C}}^n}{\Delta t} &= D_p \left(\mathrm{div}^\tau \nabla^{\mathcal{D}} u^{\tau,n+1}\right)_{\mathrm{C}} - \tau_1 u_{\mathrm{C}}^n - \tau_{1,\mathrm{out}} (1 - u_{\mathrm{C}}^n)^2 u_{\mathrm{C}}^n \\
&\quad - \beta(A_{\mathrm{C}}^n) \left(\nabla^\tau \rho^{\tau,n}\right)_x \qquad (2.6b) \\
\frac{v_{\mathrm{C}}^{n+1} - v_{\mathrm{C}}^n}{\Delta t} &= D_p \left(\mathrm{div}^\tau \nabla^{\mathcal{D}} v^{\tau,n+1}\right)_{\mathrm{C}} - \tau_1 v_{\mathrm{C}}^n - \tau_{1,\mathrm{out}} (1 - v_{\mathrm{C}}^n)^2 v_{\mathrm{C}}^n \\
&\quad - \beta(A_{\mathrm{C}}^n) \left(\nabla^\tau \rho^{\tau,n}\right)_y \qquad (2.6c) \\
\frac{A_{\mathrm{C}}^{n+1} - A_{\mathrm{C}}^n}{\Delta t} &= D_A \left(\mathrm{div}^\tau \nabla^{\mathcal{D}} A^{\tau,n+1}\right)_{\mathrm{C}} - a_{1,C} A_{\mathrm{C}}^n - a_{1,\mathrm{out}} (1 - \rho_{\mathrm{C}}^n)^2 A_{\mathrm{C}}^n \\
&\quad + \rho_{\mathrm{C}}^n a_{0,\mathrm{C}} \left((u_{\mathrm{C}}^n)^2 + (v_{\mathrm{C}}^n)^2\right) \qquad (2.6d)
\end{aligned}$$

We complete this scheme with homogeneous Dirichlet boundary conditions on the boundary cells $\mathrm{C} \in \partial\mathcal{M} \cup \partial\mathcal{M}^*$:

$$\rho_{\mathrm{C}}^n = 0, \qquad u_{\mathrm{C}}^n = 0, \qquad v_{\mathrm{C}}^n = 0, \qquad A_{\mathrm{C}}^n = 0. \qquad (2.7)$$

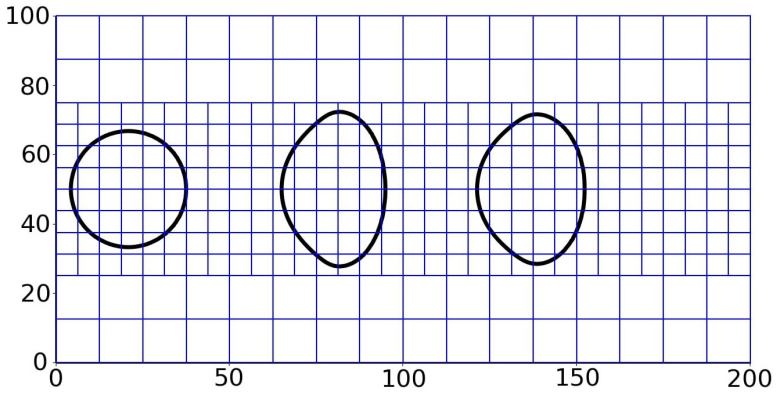

FIGURE 3. Example of cell moving on a locally refined mesh at the center of the discretization domain. At this level of refinement, the space step in the coarse (resp. fine) zone is equal to 12.5 (resp. 6.25).

The domain Ω is in what follows given by $[0, 200] \times [0, 100]$. Most of the simulations are done on a refined version of the mesh shown in Figure 3, where each cell is divided in 4, 3 times (thus the "space step" is divided by 64). In the case where the initial position of the cell are not located in the center left of the domain, we use classical cartesian meshes, with the fine space step. The time step is taken equal to 10^{-2}. For all the simulations that follow, we are in one of two situation. For numerical grids $[0, 200] \times [0, 100]$, the x-label is x and the y-label is y. Otherwise, the figure is just to visualize the shape of the cell and/or the distribution of certain quantities like $\vec{p}$ or A_{dh} relatively to the cell position.

3. Classical and reverse adhesive haptotaxis in silico

3.1. Simulations on homogeneous adhesive substrate

Let us refer to *homogeneous substrates* when the parameters of detachment of adhesion links $a_1(x, y)$ and creation of adhesion links $a_0(x, y)$ are constant and independent of space. The adhesiveness of these homogeneous substrates varies according to the values taken by these parameters. Let us fix the adhesion creation parameter at a constant value $a_0 = 0.025$ and focus on the influence of the parameter a_1. Increasing the value of a_1 decreases the adhesiveness properties of the substrate. It is then interesting to study the impact of a_1 on cell movement. Analogous behavior has been observed for adhesion bands generated by the parameter a_0. Results are reported in Appendix B.

Here and in the following we take a circular initial condition ρ_0 defined by:

$$\rho_0(x, y) = \frac{1}{2}\left(1 - \tanh\left(\kappa\left((x - x_0)^2 + (y - y_0)^2 - r_0^2\right)\right)\right)$$

The parameter $r_0 \in \mathbb{R}_+$ is the initial radius of the cell, and the pair $(x_0, y_0) \in \mathbb{R}^2$ is the initial center of mass of the cell. The membrane thickness is controlled non trivially by κ and r_0, where an increasing κ tends to diminish the membrane thickness.

The initial condition $\overrightarrow{p_0}$ is set to:

$$\overrightarrow{p_0}(x, y) = \begin{cases} \begin{pmatrix} 1 \\ 0 \end{pmatrix} & \text{if } \rho_0(x, y) \neq 0 \\ \begin{pmatrix} 0 \\ 0 \end{pmatrix} & \text{if } \rho_0(x, y) = 0 \end{cases}$$

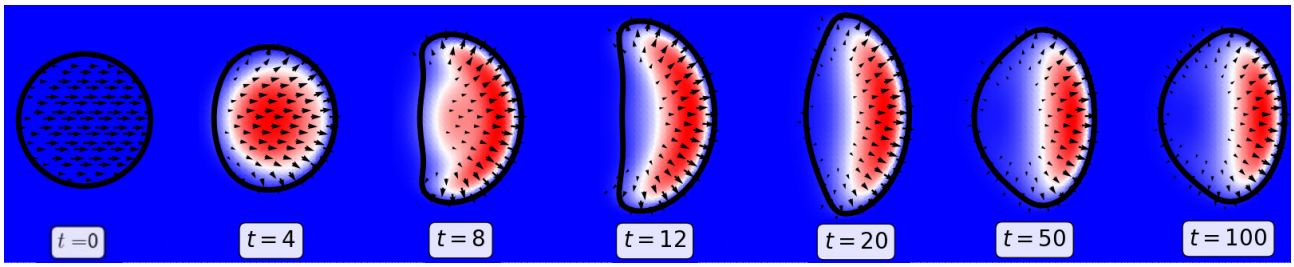

FIGURE 4. Simulation of Model (2.2) with parameters from Table 1, on the homogeneous substrate defined by $a_0 = 0.025$ and $a_1 = 0.3$. Visualization of the variable A_{dh} at times $t = 0$, $t = 4$, $t = 8$, $t = 12$, $t = 20$, $t = 50$ and $t = 100$, together with $\overrightarrow{p}$ represented by the arrows, and the contour line $\rho = 0.25$.

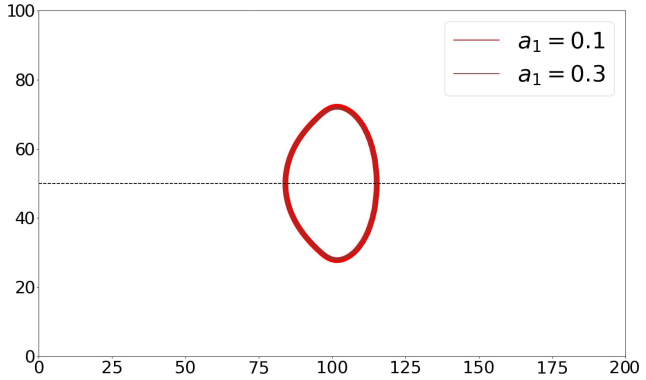

(A) Visualization of the contour of ρ for the level line $\rho = 0.25$ at time $t = 60$.

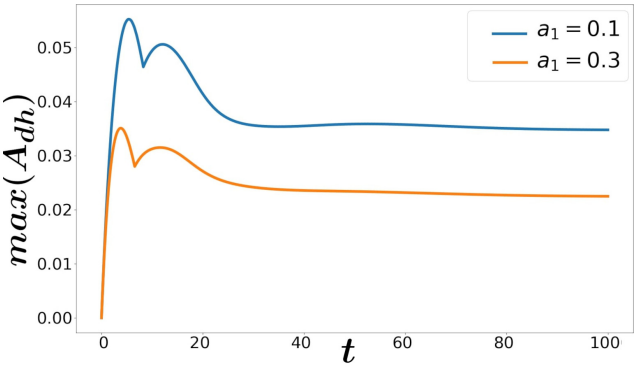

(B) Curve of $t \mapsto \max_{x,y\in\Omega}(A_{dh}(t,x,y))$

FIGURE 5. Simulation of Model (2.2) for parameter Table 1, on two different homogeneous substrates corresponding to parameters $a_1 = 0.1$ and $a_1 = 0.3$.

This means that the cell is initially pushed to the right in the simulations.

Let us start with an homogeneous substrate defined with $a_1 = 0.3$. Figure 4 shows the time evolution of the cell shape, the mean actin orientation and the adhesion density A_{dh}. Red zone corresponds to high densities of adhesion links whereas blue zones corresponds to areas without adhesion links. High adhesion densities are located at the front of the cell, which correlates with the fact that these are the areas where $|\overrightarrow{p}|^2$ was highest (corresponding to long arrows). The motion displayed can be split in two phases, in accordance with results from [7]: first the cell breaks its circular symmetry to adopt a polarized fan-like shape, and then a persistent motion occurs to the right of the domain. The same simulation can be performed with $a_1 = 0.1$. In Figure 5, we confront this result with the previous one. The overall behavior of the simulation is identical: we observe cell movement with persistent motion along a horizontal axis.

In Figure 5a, we see that for $a_1 = 0.1$, the contour line $\rho = 0.25$ coincide for both value $a_1 = 0.1$ and $a_1 = 0.3$. This means that the adhesiveness of the substrate has a negligible effect on the overall velocity of the cell. This is in remarkable agreement with experiments that show an independence of cell velocity in a wide range of adhesion conditions [3, 26]. This consistence may be explained by the fact that in the model and the experiments cell velocity is controlled by actin polymerization dynamics and not by contractility nor cell detachment in trailing edge that are both negligible experimentally and neglected in the model.

However, the high adhesion density at the front of the cell varies according to the parameter a_1 : decreasing the adhesion detachment parameter results in an overall increase in the function $t \to \max_{x,y\in\Omega}(A_{dh}(t,x,y))$, as

seen in Figure 5b. Furthermore, we observed that $t \to \max_{x,y\in\Omega}(A_{dh}(t,x,y))$ has a non monotonous behavior in the symmetry breaking phase, while it stabilizes in the persistent motion phase.

3.2. Simulations on inhomogeneous adhesive substrate

Let's consider the case of experiments perfomed in LAI, where lymphocytes migrate on substrates patterned with stripes of different adhesiveness [3, 26]. In our model, we define two horizontal bands of equal size but different adhesiveness, covering the upper and lower halves of the domain. To align with the color code of LAI experiments (Fig. 2), we create a low adhesion band (in brown) and a high adhesion band (in red). The high adhesion zone corresponds to an area where $a_1^h < a_1^l$. Here, we have $a_1^h = 0.1$ while the low adhesion zone corresponds to $a_1^l = 0.3$. The parameter a_1 is thus piecewise constant:

$$a_1(x,y) = \begin{cases} a_1^l \text{ if } y > 50, \\ a_1^h \text{ if } y \leq 50. \end{cases} \tag{3.1}$$

Let us use the previous adhesiveness setting to understand how to generate *in silico* reverse adhesive haptotaxis phenomenon on inhomogeneous substrates. Recall that the adhesion dynamics is coupled to the cell dynamics through two different coupling terms, $-\alpha(A_{dh})\overrightarrow{p}\cdot\nabla\rho$ in (2.2a) and $-\beta(A_{dh})\nabla\rho$ in (2.2b). We say that a coupling term is *activated* when the respective function α or β is non constant. At initial time, the cell straddles both zones (same initial condition for ρ and $\overrightarrow{p_0}$ than in the previous section).

3.2.1. Classical adhesive haptotaxis

We first consider the case where only the coupling *via* polymerization is activated and positive, *i.e.* $\beta_1 > 0$ in the term $\beta(A_{\mathrm{dh}})$ (and $\alpha_1 = 0$ in the term $\alpha(A_{dh})$). In Figure 6, we observe a similar deformation phase as in Figure 4, but this time, the cell gradually moves towards the strong adhesion band. In Figure 7, we see that this behavior is generic: for several parameter pairs (α_0, β_0), the trajectories of the centers of mass systematically move towards the strong adhesion band. Thus, the classic adhesive haptotaxis guidance phenomenon is generated when the adhesion density promotes polymerization. Moreover, if we observe the variables A_{dh} and $\vec{p}$ at time $t = 20$ in Figure 6 (right), we see that A_{dh} is concentrated in the area of high adhesion. Moreover, examining the variables A_{dh} and $\vec{p}$ at time $t = 20$ in Figure 6 (right), we observe that A_{dh} is highly concentrated in the region of high substrate adhesion—consistent with the expectation that stronger ligand density promotes increased adhesion. At the same time, $\vec{p}$ is significantly elevated in the lower part of the cell, reflecting a positive feedback between adhesion and polymerization. This spatial configuration promotes enhanced protrusive activity at the cell edge in the high-adhesion zone, thereby driving cell spreading in that region. As a result, the cell exhibits the classical haptotaxis phenotype.

3.2.2. Reverse adhesive haptotaxis

Now we consider the case where the coupling through the propulsion term is the only one activated and positive *i.e.* $\alpha_1 > 0$ in the term $\alpha(A_{\mathrm{dh}})$ (and $\beta_1 = 0$ in the term $\beta(A_{dh})$).

We still observe in Figure 8, that the cell deforms as previously, but this time it is attracted towards the low adhesion zone. This behavior matches what has been experimentally observed in Figure 2, which is termed reverse adhesive haptotaxis. This behavior remains consistent even when varying the coupling parameters (α_0, β_0) as can be seen in Figure 9. The trajectory of the center of mass consistently moves towards the low adhesion band. Figure 8 (right) displays the variable A_{dh} and $\overrightarrow{p}$ at time $t = 20$. While A_{dh} is still more present in high adhesion area, its intensity in the low adhesion area is more important than in the case of classical haptotaxis. The amplitude of $\overrightarrow{p}$ do not display any major difference in this case that could explain this non-classical phenomenon of reverse haptotaxis. Figure 8 (right) shows the variables A_{dh} and $\vec{p}$ at time $t = 20$. Compared to the previous case involving positive feedback between adhesion and polymerization (Fig. 6, right), the asymmetry in both A_{dh} and $\vec{p}$ is much less pronounced. Although some asymmetry remains—suggesting

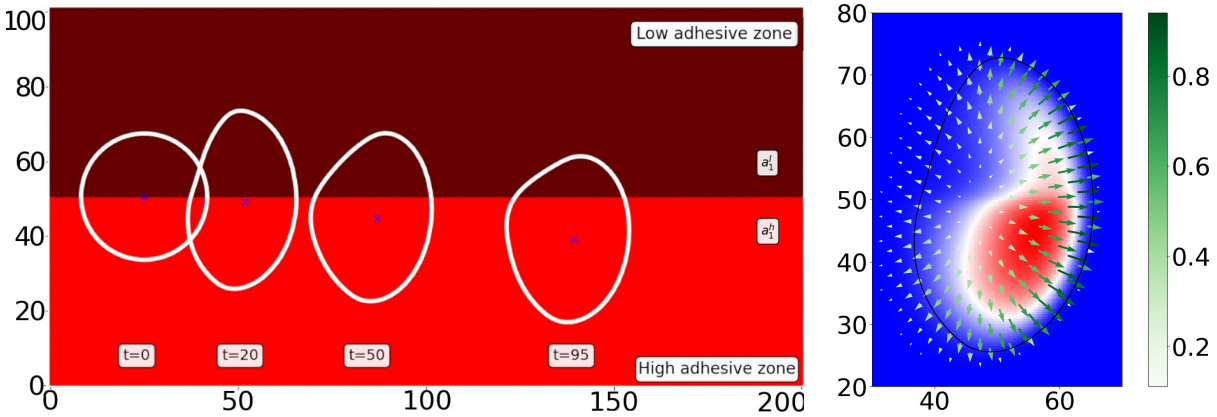

FIGURE 6. Left: simulation of Model (2.2) for parameter Table 1, with two adhesive bands defined by $a_1^h = 0.1$ for the strong adhesion zone and $a_1^l = 0.3$ for the weak adhesion zone. The adhesion creation parameter is $a_0^h = a_0^l = 0.025$. The coupling with actin polymerization is activated by $\beta_1 = 30$, and the coupling with propulsion is deactivated by $\alpha_1 = 0$. Visualization of the contour of ρ for the level line $\rho = 0.25$. Right: Visualization of variables A_{dh} and $\vec{p}$ at time $t = 20$ for the simulation presented on the left. High values of the variable A_{dh} are represented in red (max $A_{dh} = 0.059$) , whereas values close to 0 are in blue and intermediate values in white. Colorbar is mapped to the length of $\vec{p}$.

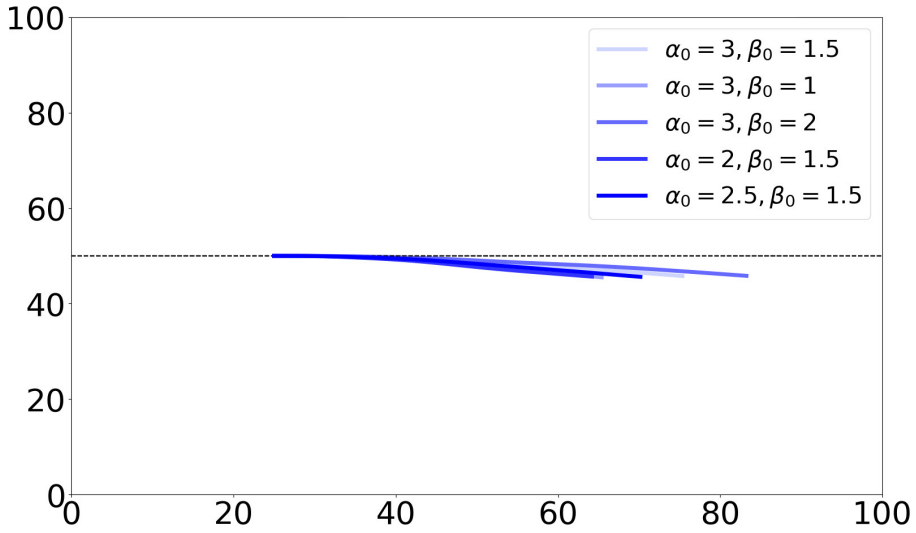

FIGURE 7. Simulation of Model (2.2) for parameter Table 1, with two adhesive bands defined by $a_1^h = 0.1$ for the strong adhesion zone and $a_1^l = 0.3$ for the weak adhesion zone. The adhesion creation parameter is $a_0^h = a_0^l = 0.025$. The coupling with actin polymerization is activated by $\beta_1 = 30$, and the coupling with propulsion is deactivated by $\alpha_1 = 0$. Visualization of the trajectory of the cell's center of mass up to time $t = 40$, for multiple parameters α_0 and β_0.

that classical haptotaxis might still be expected, albeit weaker—the observed emergence of a pronounced reverse haptotaxis phenotype warrants further investigation. A notable difference between Figure 6 (right) and Figure 8 (right) provides a potential explanation. In Figure 6, the vector field $\vec{p}$ shows high intensities all along the cell edge within the high-adhesion region, including the bottom and rear of the cell. This widespread polymerization

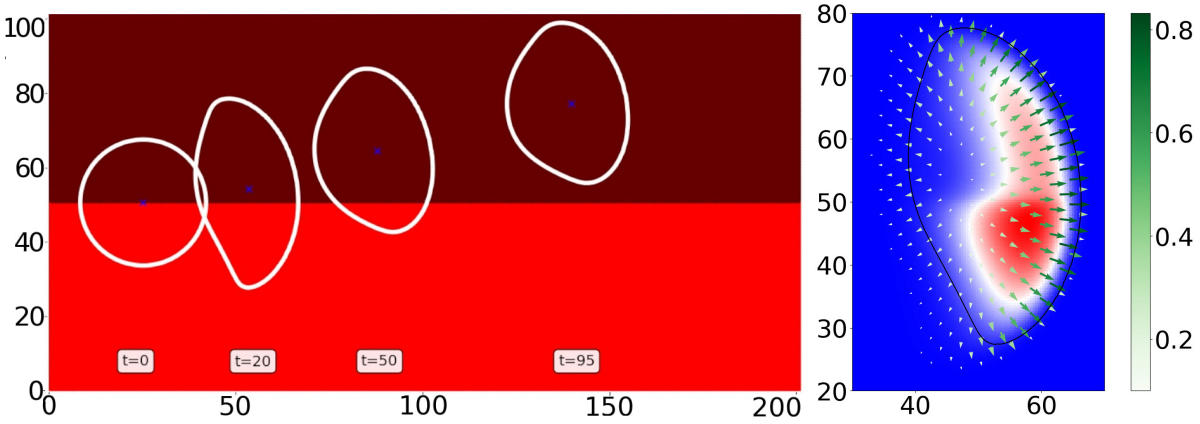

FIGURE 8. Left: simulation of Model (2.2) for parameter Table 1, with two adhesive bands defined by $a_1^h = 0.1$ for the strong adhesion zone and $a_1^l = 0.3$ for the weak adhesion zone. The adhesion creation parameter is $a_0^h = a_0^l = 0.025$. The coupling with propulsion is activated by $\alpha_1 = 30$, and the coupling with actin polymerization is deactivated by $\beta_1 = 0$. Visualization of the contour of ρ for the level line $\rho = 0.25$. Right: visualization of variables A_{dh} (from 0 in blue to 0.0398 for max A_{dh} in red) and $\vec{p}$ at time $t = 20$ for the simulation presented in the left (colorbar is associated to $\vec{p}$).

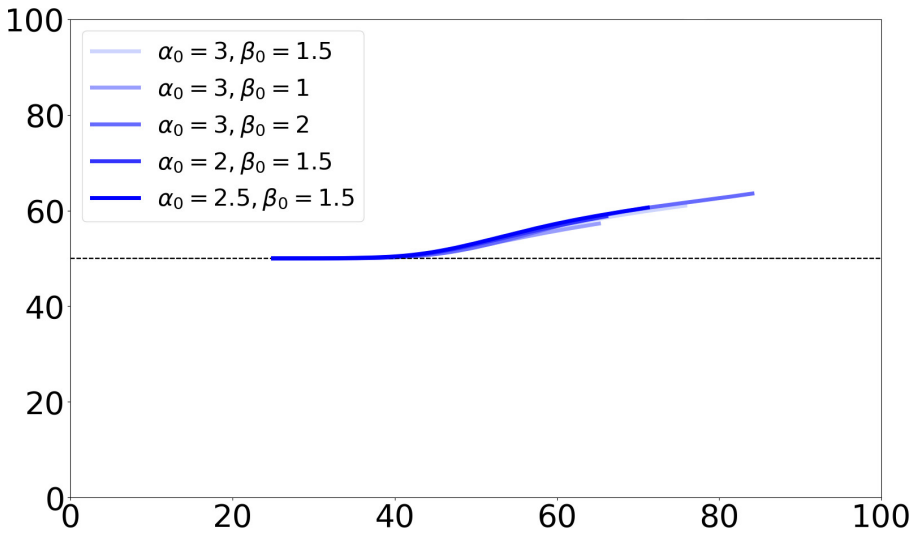

FIGURE 9. Simulation of Model (2.2) for parameter Table 1, with two adhesive bands defined by $a_1^h = 0.1$ for the strong adhesion zone and $a_1^l = 0.3$ for the weak adhesion zone. The adhesion creation parameter is $a_0^h = a_0^l = 0.025$. The coupling with propulsion is activated by $\alpha_1 = 30$, and the coupling with actin polymerization is deactivated by $\beta_1 = 0$. Visualization of the trajectory of the cell's center of mass up to time $t = 40$, for multiple parameters α_0 and β_0.

promotes strong spreading across the adhesive zone, suggesting that the cell is "drawn into" or effectively adsorbed by the high-adhesion area. In contrast, Figure 8 (right) shows that $\vec{p}$ is concentrated primarily at the leading edge of the cell, without marked asymmetry between the left and right sides, so that the cell maintains an overall symmetric shape along its main migration axis and behaves more like a rigid or "solid" body. In

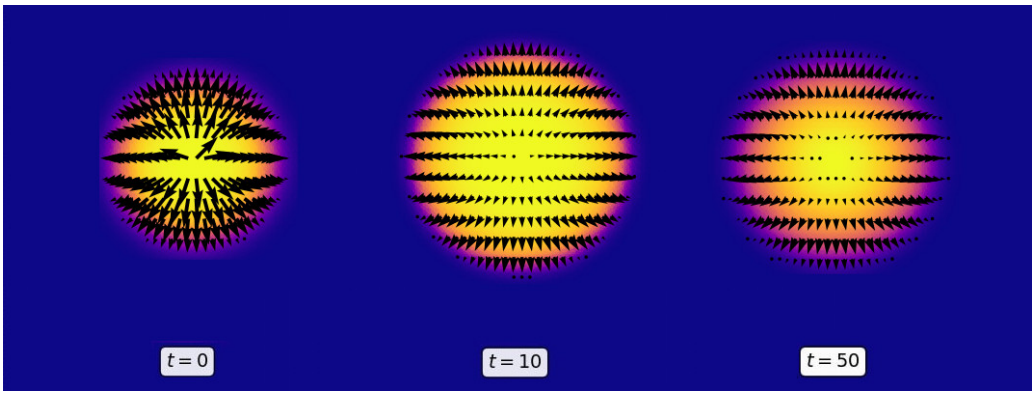

FIGURE 10. Time evolution of the cell shape and the vector field $\vec{p}$ for an initial condition $\vec{p}_0$ radially symmetric. Yellow represents the inside of the cell while blue is the outside, separated by the membrane. Note that the cell center of mass stays at the same location. Coupling conditions are $\alpha_1 = 30$ and $\beta_1 = 0$ to have reverse haptotaxis.

this context, the differential in edge velocity resulting from propulsion coupling generates a torque that induces rotation of the cell rigid body toward the left, leading to reverse haptotaxis.

3.2.3. Impact of the initial condition of mean orientation

Let us investigate the impact of the initial conditions $\overrightarrow{p_0}$ on the cell displacement.

First, if $\overrightarrow{p_0}$ is radially symmetric, we can see in Figure 10 that the cell first expands and then retracts towards a stable circular shape. The radial symmetry is preserved all along the computation, and there is no motion, as expected from symmetrical arguments and as observed for active cells that display no front-rear polarization. Non motile case is however unstable in the model and limited to perfect circular symmetry.

Secondly, we choose an initial condition $\overrightarrow{p_0}$ of the form:

$$\overrightarrow{p_0}(x,y) = \begin{cases} \begin{pmatrix} 1 \\ 0 \end{pmatrix} & \text{if } \rho_0(x,y) \neq 0 \text{ and } x > 50 \\ \begin{pmatrix} -p_l \\ 0 \end{pmatrix} & \text{if } \rho_0(x,y) \neq 0 \text{ and } x < 50 \\ \begin{pmatrix} 0 \\ 0 \end{pmatrix} & \text{if } \rho_0(x,y) = 0 \end{cases} \tag{3.2}$$

with $p_l \geq -1$ to distinguish clearly the front from the rear ($p_l < -1$ would simply reverse that distinction).

On a homogeneous substrate, the deformation of the cell depends deeply on the value of the parameter p_l. We see in Figure 11 (top), that for low values of p_l, the deformation is similar to the case $p_l = -1$ as used in Figure 4. When p_l increases, we observe a wide deformation of the rear of the cell for intermediate times. For large time, the cell adopts for the largest values of p_l a round shape. This behavior is similar to behavior of some cells in experiments (Fig. 11 (bottom)).

On an inhomogeneous substrate, we observe in Figure 12 for $p_l = 0.5$ a larger deformation of the rear cell with a classical (resp. reverse) adhesive haptotaxis for a coupling by the actin polymerization (resp. propulsion). If we compare the results for reverse haptotaxis (bottom of Fig. 12) to the one in Figure 8 (left), we observe also a later move to the low-adhesion zone.

Finally, we investigate the case of an initial condition $\overrightarrow{p_0}$ whose polarization is transverse to the interface between the two bands, oriented towards the highest adhesive band. Figure 13 shows that in that case, reverse

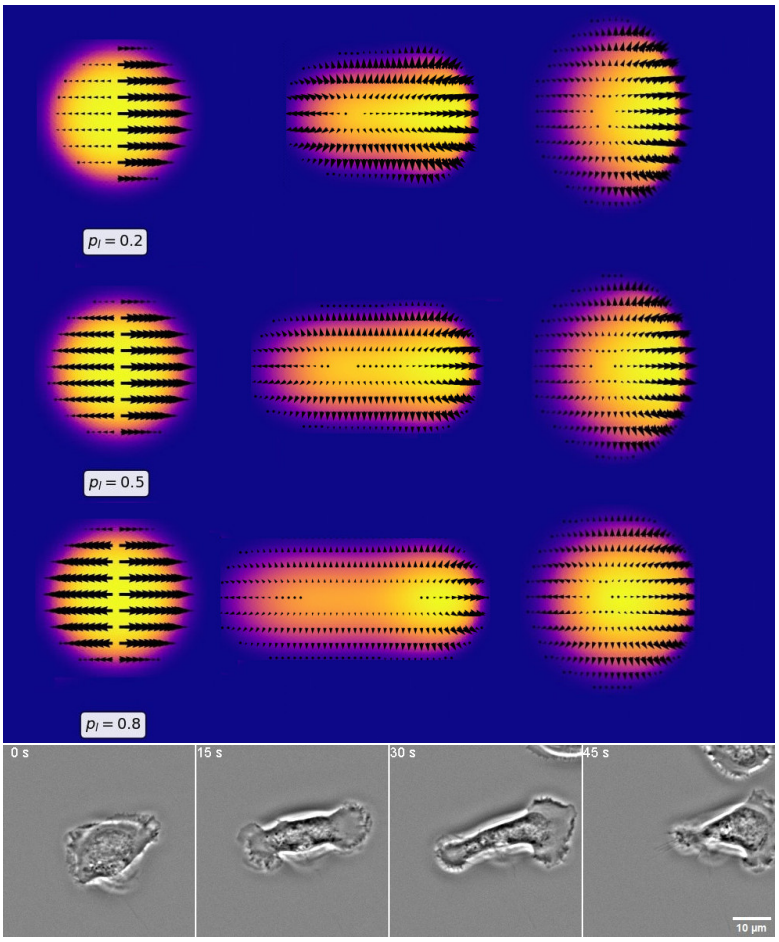

FIGURE 11. Top: evolution of the cell shape and the vector field $\vec{p}$ for different value of p_l. Left column correspond to the initial condition. Center column corresponds to intermediate times depending on the value of p_l. Right column corresponds to the time $t = 50$. Bottom: effector T cell migrating on a substrate coated with ICAM-1.

haptotaxis does not occur. It would be of great interest to capture a ratio of signaling/polarization to be able to invert this behavior.

3.2.4. Transition in adhesive haptotaxis

In the previous discussion, we saw that the two types of adhesion dynamics coupling allow us to generate two types of adhesive haptotaxis: one directed towards areas of higher adhesion when the coupling on the polymerization term is activated, and the other directed towards areas of lower adhesion when the coupling on the propulsion term is activated. Let us study the case where both coupling are activated simultaneously.

To interpret our results, let us introduce a function called ID (for *Index of Deviation*), which is defined as follows:

$$\mathrm{ID}(t; \alpha_1, \beta_1) = 50 - y_{cen}(t) \tag{3.3}$$

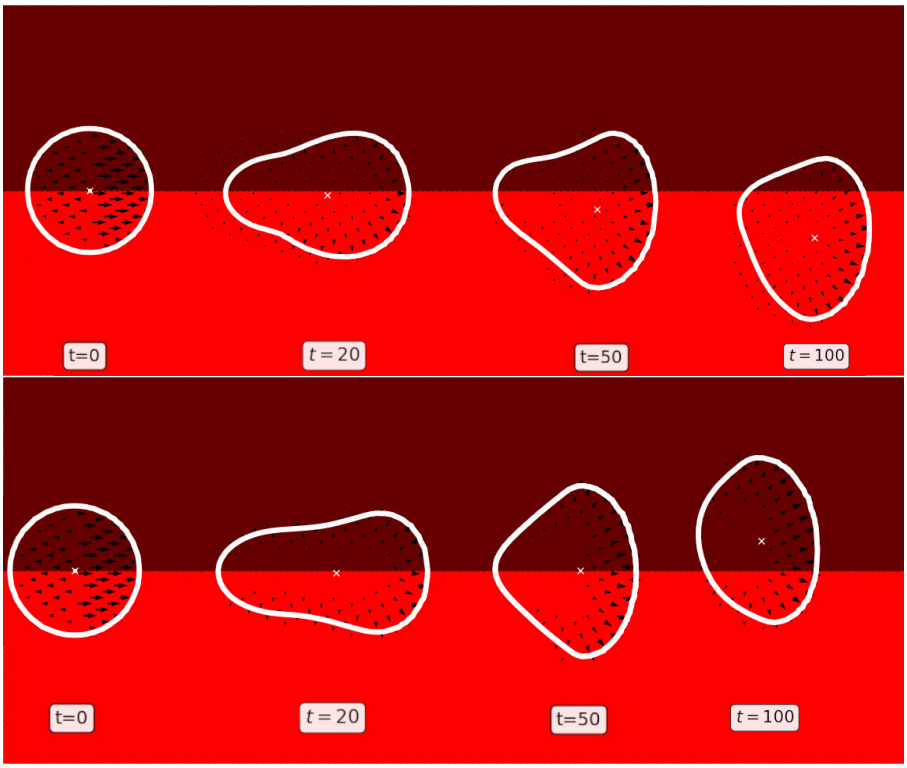

FIGURE 12. Simulation of Model (2.2) for parameter Table 1 and the initial condition (3.2) for $\vec{p}_0$ with $p_l = 0.5$. On top, the coupling with actin polymerization is activated by $\beta_1 = 30$, and on the bottom coupling with propulsion is activated by $\alpha_1 = 30$. Visualization of the contour of ρ for the level line $\rho = 0.25$.

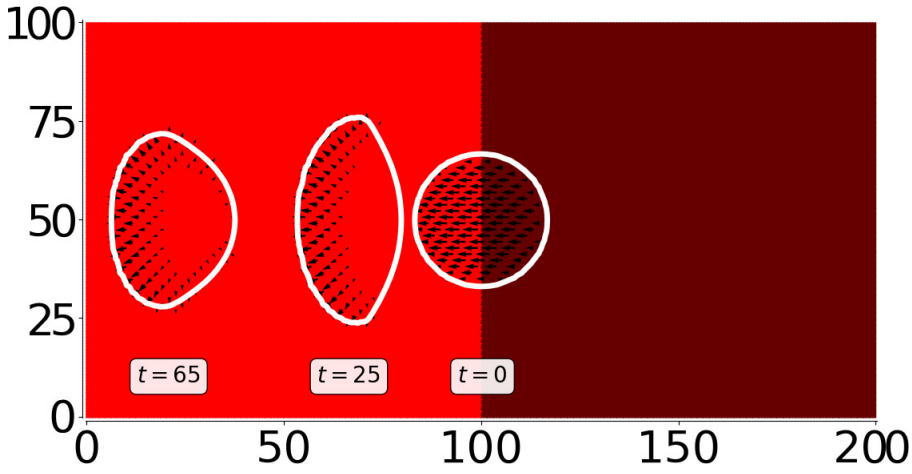

FIGURE 13. Simulation of Model (2.2) for parameter Table 1 and initial condition $\vec{p}_0$ with an orientation transverse to the to the adhesive bands. The coupling is activated by propulsion with $\alpha_1 = 30$. Visualization of the contour of ρ for the level line $\rho = 0.25$.

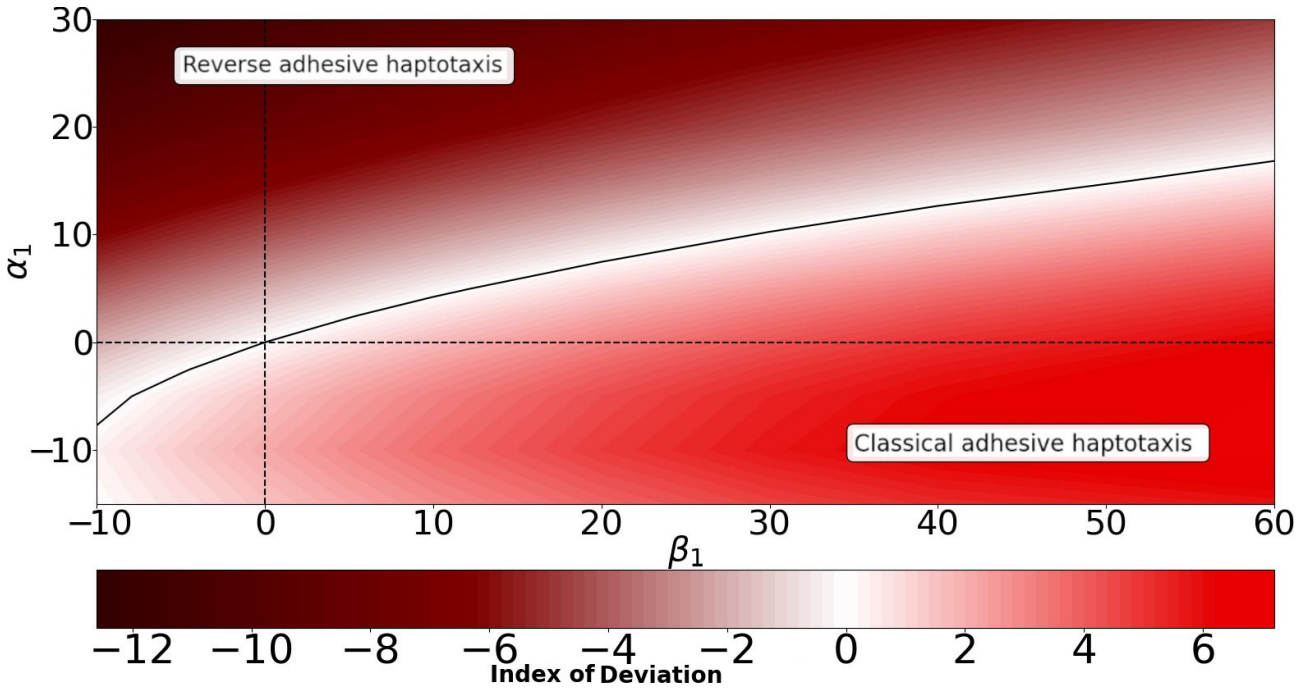

FIGURE 14. Heatmap of the ID function for the parameter Table 1, at time $t = 40$, and for parameters $\alpha_0 = 3$ and $\beta_0 = 1.5$. The zero contour line of the ID function separating classical haptotaxis from inverse haptotaxis is marked by the black curve.

where $t \mapsto y_{cen}(t)$ stands for the time evolution of vertical coordinate of the center of mass of the cell. This function calculates, for a time $t > 0$, the deviation between the cell's center of mass and the interface separating the two adhesive bands (which lies at $y = 50$ in our simulation). It depends on all the parameters of the problem, but we focus on the dependence on the coupling parameters α_1 and β_1. When both couplings are activated simultaneously, we expect to observe one of the two types of adhesive haptotaxis. The ID function helps us to detect the nature of the resulting adhesive haptotaxis. If the cell enters the area of higher adhesion, we get $\mathrm{ID}(t, \alpha_1, \beta_1) > 0$ whereas if it moves towards the band of lower adhesion, we have $\mathrm{ID}(t, \alpha_1, \beta_1) < 0$. This indicator is also quantitative: the higher its amplitude, the more pronounced the deviation.

In Figure 14, the upper right part delimited by the dotted axes represents the heatmap of the function $(\alpha_1, \beta_1) \to \mathrm{ID}(40; \alpha_1, \beta_1)$ with α_1 varying between 0 and 30 and β_1 varying between 0 and 60. Negative values of ID (reverse adhesive haptotaxis) correspond to brown areas, while positive values of ID (classical adhesive haptotaxis) correspond to red areas. We observe a separation between a zone leading to classical haptotaxis and a zone leading to reverse haptotaxis, corresponding to values of ID close to 0. Based on Figure 14, we can write the zero contour line of ID as a function ψ satisfying the following relation:

$$\psi(\beta_1) = \alpha_1$$

We also notice that if $\alpha_1 = \beta_1 = 0$, that is, if adhesion density is not taken into account, then ID remains equal to zero, indicating movement without adhesive haptotaxis.

This transition zone is thus represented by the function ψ, but it also depends on other model parameters, notably α_0 and β_0, as seen in Figure 15, which shows these zero contour lines for the parameter pairs (α_0, β_0) referenced in Table 1. In particular, this function does not depend on time t: indeed, when the heatmap is plotted for a later time, it has a negligible influence on its general shape. We then notice a clear influence of the

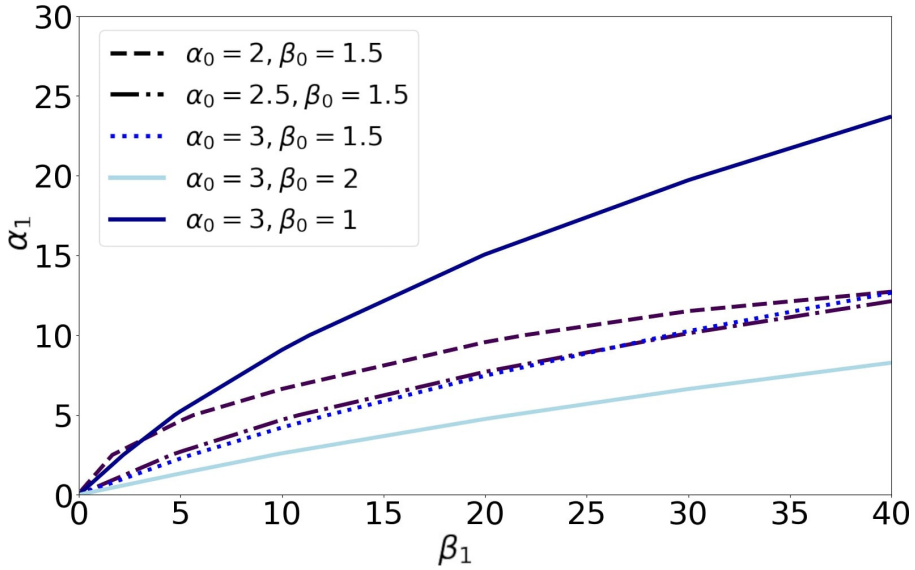

FIGURE 15. Graph of the function ψ at time $t = 40$, for the parameter Table 1 and different pairs of parameters (α_0, β_0), for two adhesive bands defined by $a_1^h = 0.1$ for the high adhesion area and $a_1^l = 0.3$ for the low adhesion area.

parameter β_0, with an increase in the classical adhesive haptotaxis zone as the parameter decreases (blue curves in the graph). The impact of the propulsion parameter α_0 is much less significant: the three chosen parameters yield very similar curves (dashed curves in the graph), and the amplitude of the ID function values being very close does not allow distinguishing an effect of this parameter.

We can raise one last issue concerning these two couplings: while the impact of these couplings on adhesion dynamics has been studied exclusively through the effect of positive coupling parameters (α_1, β_1), what happens if this consideration is made through negative coupling parameters? In other words, how does an impact of adhesion dynamics through a deceleration of propulsion or depolymerization affect the model?

To conduct this study, it is necessary to always preserve $\alpha(A_{dh}) > 0$ and $\beta(A_{dh}) > 0$, so the parameters $\alpha_1 < 0$ and $\beta_1 < 0$ must be taken within a limit that satisfies this constraint. We observe in the bottom left, bottom right and upper left parts of Figure 14 delimited by the dotted axes that the heatmap completed with these negative coupling parameters reveals new results. For instance, if $\alpha_1 = 0$ (see the horizontal axis drawn on the graph), a change in the sign of β_1 leads to a change in the type of haptotaxis: while $\beta_1 > 0$ leads to classical adhesive haptotaxis, $\beta_1 < 0$ results in reverse adhesive haptotaxis. Similarly, when $\beta_1 = 0$ (see the vertical axis drawn on the graph): while $\alpha_1 > 0$ leads to reverse adhesive haptotaxis, $\alpha_1 < 0$ results in classical adhesive haptotaxis.

4. Conclusion and perspectives

Extending the model of [5, 6] with a coupling between adhesion and polymerization allowed us to generate the two types of adhesive haptotaxis, classical and reverse. The discretization of our model produced simulations of cells moving on heterogeneous bands reproducing the experimental observations of [3] for lymphocytes amoeboid migration. Our model is based on two strong and somewhat unconventional assumptions, inspired by experimental studies of integrin LFA-1–mediated amoeboid motility in lymphocytes [3, 8]: (i) that contractility plays only a marginal role in the propulsion mechanism, and (ii) that adhesion is spontaneously lost and largely negligible for motility. These assumptions are inherently built into our model and are indirectly supported by the fact that it captures key experimental features of LFA-1–mediated lymphocyte migration—most

notably, the apparent independence of cell velocity from substrate adhesiveness, and the evolution of cell shape involving retraction of multiple lobes. However, our model is less suited for describing lymphocyte migration mediated by other adhesion molecules such as VLA-4, where adhesion at the cell rear has been shown to play a significant role in propulsion and guidance [3, 27]. Furthermore, we found that haptotaxis was classical by positive signaling on polymerization and reverse by positive signaling on propulsion. Conversely, negative signaling on either process produces the opposite effect. When both effects were taken into account, a transition zone could be identified between classical haptotaxis to reverse haptotaxis in the plane α_1 and β_1. Interestingly, our model reveals two distinct mechanistic pathways for cell reorientation. Coupling to polymerization appears to drive reorientation *via* asymmetric spreading of the cell's lateral edges, resulting in a transient but pronounced asymmetry in cell shape. This behavior closely resembles the biosignaling-driven mechanism proposed for mesenchymal cells ([2]). In contrast, coupling to propulsion induces reorientation through a solid-like rotation of the cell body, generated by torque arising from differences in the lateral edge velocities. This alternative scenario provides a mechanistically distinct explanation for experimental observations of cell reorientation. It may motivate new investigations in experimental systems, although direct biological evidence for localized coupling between adhesion and edge propulsion remains limited. Moreover, since positive and negative coupling produce opposite haptotaxis phenotypes, classical haptotaxis arises from either positive coupling to polymerization or negative coupling to propulsion. Conversely, reverse haptotaxis arises from positive coupling to propulsion or negative coupling to polymerization. Hence, our model does not provide a direct link between a haptotaxis phenotype either classical or reverse, and a precise mechanistic explanation. Experimentally, both enhancement (*e.g.*, lymphocytes [2]) and inhibition (*e.g.*, keratocytes [28]) of cell front advancement due to substrate adhesion have been reported, and it remains challenging to determine whether these effects arise from differential spreading—corresponding to polymerization coupling in our model—or solid-cell body rotation, corresponding to propulsion coupling in our model. One potential distinguishing feature suggested by our model is the transient asymmetry in cell shape observed during rotation. However, this remains a qualitative indicator and may only be detectable under sharp, step-like changes in adhesion, becoming much less apparent in smoother adhesion gradients. In any case, further experimental investigation is necessary to elucidate the mechanisms linking adhesion and propulsion—particularly in lymphocytes, which remain the only known system to exhibit reverse haptotaxis. Also, while our minimal model captures the main trends of lymphocyte haptotaxis, future efforts should aim at developing more refined models to achieve greater precision and to better account for cell behavior in complex and dynamic adhesion landscapes."

Acknowledgments

The project leading to this publication has received funding from France 2030, the French Government program managed by the French National Research Agency (ANR-16-CONV-0001) and from Excellence Initiative of Aix-Marseille University - A*MIDEX. Centre de Calcul Intensif d'Aix-Marseille is acknowledged for granting access to its high performance computing resources.

Data availability statement

The code used in this paper is available online in a Github repository: https://github.com/LucasCurci-mathematics/haptotaxis-adh/ [29].

References

[1] S.B. Carter, Principles of cell motility: the direction of cell movement and cancer invasion. *Nature* **208** (1965) 1183–1187.

[2] S.J. King, S.B. Asokan, E.M. Haynes, S.P. Zimmerman, J.D. Rotty, J.G. Alb, A. Tagliatela, D.R. Blake, I.P. Lebedeva, D.Marston, H.E. Johnson, M.Parsons, N.E. Sharpless, B. Kuhlman, J.M. Haugh, and J.E. Bear. Lamellipodia are critical for haptotactic sensing and response. *J. Cell Sci.* **129** (2016) 2329–2342.

[3] X. Luo, V.S. de Noray, L. Aoun, M. Biarnes-Pelicot, P.-O. Strale, V. Studer, M.-P. Valignat and O. Théodoly, Lymphocytes perform reverse adhesive haptotaxis mediated by LFA-1 integrins. *J. Cell Sci.* **133** (2020) jcs242883.

[4] L. Aoun, A. Farutin, N. Garcia-Seyda, P. Nègre, M. Suhail Rizvi, S. Tlili, S. Song, X. Luo, M. Biarnes-Pelicot, R. Galland, J.-B. Sibarita, A. Michelot, C. Hivroz, S. Rafai, M.-P. Valignat, C. Misbah and O. Theodoly, Amoeboid swimming is propelled by molecular paddling in lymphocytes. *Biophys. J.* **119** (2020) 1157–1177.

[5] J. Löber, F. Ziebert and I.S. Aranson, Modeling crawling cell movement on soft engineered substrates. *Soft Matter* **10** (2014) 1365–1373.

[6] F. Ziebert and I.S. Aranson, Effects of adhesion dynamics and substrate compliance on the shape and motility of crawling cells. *PLoS One* **8** (2013) 1–14.

[7] F. Ziebert, S. Swaminathan and I.S. Aranson, Model for self-polarization and motility of keratocyte fragments. *J. Roy. Soc. Interface* **9** (2012) 1084–1092.

[8] L. Aoun, P. Nègre, C. Gonsales, V.S. de Noray, S. Brustlein, M. Biarnes-Pelicot, M.-P. Valignat and O. Theodoly, Leukocyte transmigration and longitudinal forward-thrusting force in a microfluidic transwell device. *Biophys. J.* **120** (2021) 2205–2221.

[9] P. Robert, M. Biarnes-Pelicot, N. Garcia-Seyda, P. Hatoum, D. Touchard, S. Brustlein, P. Nicolas, B. Malissen, M.-P. Valignat and O. Theodoly, Functional mapping of adhesiveness on live cells reveals how guidance phenotypes can emerge from complex spatiotemporal integrin regulation. *Front. Bioeng. Biotechnol.* **9** (2021).

[10] B. Andreianov, F. Boyer and F. Hubert, Discrete duality finite volume schemes for Leray-Lions type elliptic problems on general 2D-meshes. *Numer. Meth. PDEs* **23** (2007) 145–195.

[11] K. Domelevo and P. Omnes, A finite volume method for the Laplace equation on almost arbitrary two-dimensional grids. *M2AN Math. Model. Numer. Anal.* **39** (2005) 1203–1249.

[12] F. Hermeline, Approximation of diffusion operators with discontinuous tensor coefficients on distorted meshes. *Comput. Methods Appl. Mech. Eng.* **192** (1959) 1939–1959.

[13] F. Boyer and F. Hubert, Finite volume method for 2d linear and nonlinear elliptic problems with discontinuities. *SIAM J. Numer. Anal.* **46** (2008) 3032–3070.

[14] C. Cancès, C. Chainais-Hillairet and S. Krell, Numerical analysis of a nonlinear free-energy diminishing discrete duality finite volume scheme for convection diffusion equations. *Comput. Methods Appl. Math.* **18** (2018) 407–432.

[15] S. Delcourte and P. Omnes, A discrete duality finite volume discretization of the vorticity-velocity-pressure stokes problem on almost arbitrary two-dimensional grids. *Numer. Methods Part. Differ. Eq.* **31** (2015) 1–30.

[16] S. Krell, Stabilized DDFV schemes for stokes problem with variable viscosity on general 2D meshes. *Numer. Methods Part. Differ. Eq.* **27** (2011) 1666–1706.

[17] T. Goudon, S. Krell and G. Lissoni, DDFV method for Navier–Stokes problem with outflow boundary conditions. *Numer. Math.* **142** (2019) 55–102.

[18] C. Chainais-Hillairet, S. Krell and A. Mouton, Study of discrete duality finite volume schemes for the Peaceman model. *SIAM J. Sci. Comput.* **35** (2013) A2928–A2952.

[19] F. Hermeline, S. Layouni and P. Omnes, A finite volume method for the approximation of Maxwell equations in two space dimensions on arbitrary meshes. *J. Comput. Phys.* **227** (2008) 9365–9388.

[20] A. Handlovičová and D. Kotorová, Numerical analysis of the semi-implicit DDFV scheme for the regularized curvature driven level set equation in 2D. *Kybernetika* **49** (2013) 829–854.

[21] R. Tesson, *Modélisation de l'action des microtubules sur la migration cellulaire*. PhD thesis, Aix-Marseille Université (2017).

[22] L. Tomek and K. Mikula, Discrete duality finite volume method with tangential redistribution of points for surfaces evolving by mean curvature, ESAIM: M2an mathematical modelling and numerical analysis. *ESAIM: M2AN Math. Model. Numer. Anal.* **53** (2019) 1797–1840.

[23] V. Desveaux, *Contribution à l'approximation numérique de systèmes hyperboliques*. PhD thesis, Université de nantes (2013).

[24] F. Boyer and F. Nabet, A DDFV method for a Cahn–Hilliard/Stokes phase field model with dynamic boundary conditions. *M2AN* **51** (2017) 1691–1731.

[25] L. Curci, *Modélisation mathématique de la migration cellulaire : étude de cas atypiques d'haptotaxie adhésive*. Theses, Aix-Marseille Université (2024).

[26] V.S. de Noray, *Etude quantitative du guidage cellulaire dans des microenvironnements contrôlés : cas atypiques de rhéotaxie et d'haptotaxie adhésive*. Theses, Aix-Marseille Université (2022).

[27] A. Hornung, T. Sbarrato, N. Garcia-Seyda, L. Aoun, X. Luo, M. Biarnes-Pelicot, O. Theodoly and M.-P. Valignat, A bistable mechanism mediated by integrins controls mechanotaxis of leukocytes. *Biophys. J.* **118** (2020) 565–577.

[28] E.L. Barnhart, J. Allard, S.S. Lou, J.A. Theriot and A. Mogilner. Adhesion-dependent wave generation in crawling cells. *Curr. Biol.* **27** (2017) 27–38.

[29] C. Lucas, Python code for the article "in silico phase-field modeling of cell directed migration towards environments of lower or higher adhesion." (2025).

Appendix A. Impact of the parameter a_1 : gradient of adhesion

In this Appendix we perform simulations on adhesion gradient-type patterns instead of adhesive bands. *In vivo*, the variation of adhesiveness properties is probably closer to what happens on this type of configuration. In the case where the substrate exhibits an adhesiveness gradient, we vary one of the two functions $a_0(x,y)$ and $a_1(x,y)$ piecewise linearly:

$$a_1(x,y) = \begin{cases} a_1^l & \text{if } y > C_1 \quad \text{(low-adhesion zone)} \\ a_1^h & \text{if } y \leq C_2 \quad \text{(high-adhesion zone)} \\ a_1^l + \frac{(y-C_1)(a_1^h - a_1^l)}{C_2 - C_1} & \text{otherwise} \quad \text{(gradient-of-adhesion zone)} \end{cases} \tag{A.1}$$

The initial condition is then placed in the center of the gradient-of-adhesion zone. Note that the width of this zone is larger than the diameter of the initial condition. As shown in Figure A.1 (left), we observe the phenomenon of classical adhesive haptotaxis again, but it occurs later than when the transition is sharp: at time $t = 95$ of the simulation on sharp bands the cell is almost entirely within the high-adhesion zone, when at the same time, on gradients, the cell is not as deep in the high-adhesion zone as can bee seen on Figure A.1 (right). Therefore, the case of adhesion bands acts as an "extreme" case of the adhesion gradient. On the left of Figure A.2, we also observe that on an adhesion gradient, and when the coupling between cell adhesion and propulsion is activated, the cell moves towards the low-adhesion zone, but on the right of the same figure, we see that this occurs slower than on sharp adhesive bands.

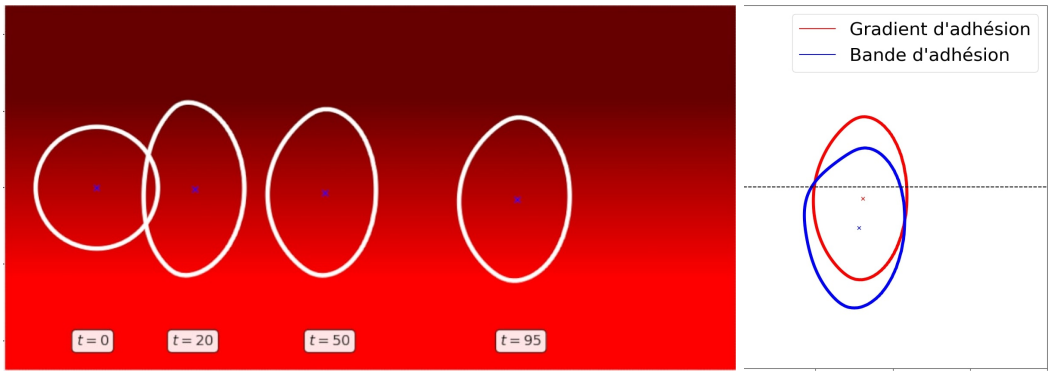

FIGURE A.1. Simulation of Model (2.2) for the Parameter Table 1, performed on an adhesion gradient between the values $a_1^h = 0.1$ and $a_1^l = 0.3$ with (A.1). The adhesion creation parameter is $a_0^h = a_0^l = 0.025$. The coupling on the polymerization term is activated with a parameter $\beta_1 = 30$ and the coupling on the propulsion term is deactivated with a parameter $\alpha_1 = 0$. On the left: visualization of the contour of ρ for the 0.25 level line at times $t = 0$, $t = 20$, $t = 50$ and $t = 95$. On the right: comparison of the contour of ρ for the 0.25 level line at time $t = 95$ on an adhesion band and on an adhesion gradient.

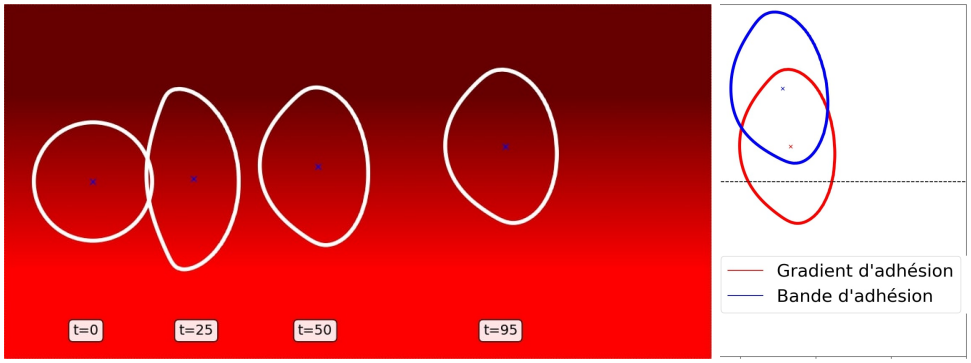

FIGURE A.2. Simulation of Model (2.2) for the Parameter Table 1, performed on an adhesion gradient between the values $a_1^h = 0.1$ and $a_1^l = 0.3$ with (A.1). The adhesion creation parameter is $a_0^h = a_0^l = 0.025$. The coupling on the propulsion term is activated with a parameter $\alpha_1 = 30$ and the coupling on the polymerization term is deactivated with a parameter $\beta_1 = 0$. On the left: visualization of the contour of ρ for the 0.25 level line at times $t = 0$, $t = 20$, $t = 50$ and $t = 95$. On the right: comparison of the contour of ρ for the 0.25 level line at time $t = 95$ on an adhesion band and on an adhesion gradient.

APPENDIX B. IMPACT OF THE PARAMETER a_0

This appendix presents additional results on Model (2.2), where we created adhesion bands or gradients not *via* the detachment parameter a_1 of (2.2c) but by varying the creation parameter $a_0(x, y)$ instead. A higher value of the creation parameter a_0 could also model an increased adhesiveness of the substrate since it is easier to create links between the cell and the substrate. Let a_0^h (resp. a_0^l) be the value of a_0 in the high-adhesion (resp. low-adhesion) zone. We thus assume that $a_0^h > a_0^l$.

We observe the same qualitative behavior when we change adhesiveness through a_0 rather than through a_1. On Figure B.1 and Figure B.2 (left), we activate the polymerization term ($\alpha_1 = 0$, $\beta_1 = 30$) and observe the classical haptotaxis, whereas on the right we activate the propulsion term ($\alpha_1 = 30$ and $\beta_1 = 0$) and observe the reverse haptotaxis.

The corresponding heatmap given in Figure B.3 and the localization of the transition front for several values of (α_0, β_0) in Figure B.4 are similar to their counterparts obtained in Section 3.

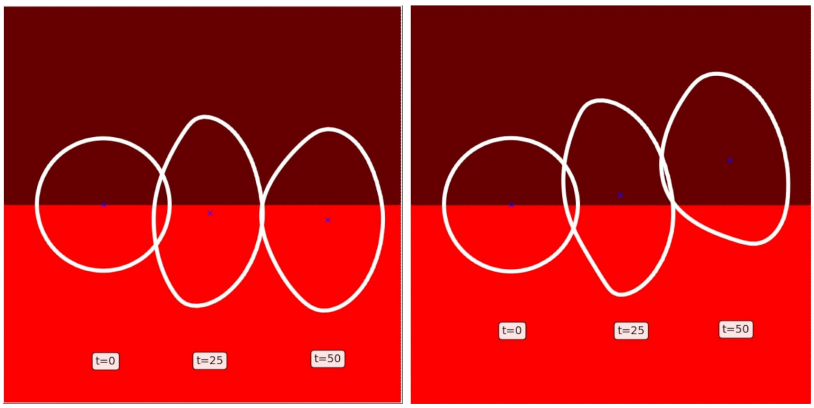

FIGURE B.1. Analogous to Figure 6 and 8 for two adhesive bands defined by $a_0^h = 0.025$ for the high adhesion zone and $a_0^l = 0.0025$ for the low adhesion zone.

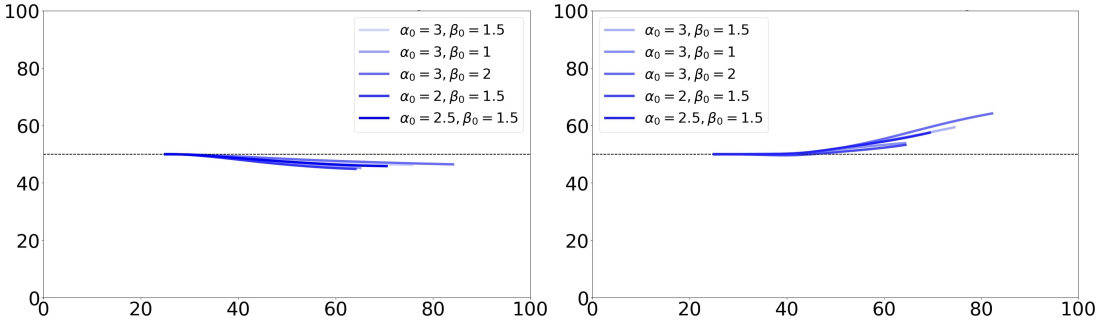

FIGURE B.2. Analogous to Figure 7 and 9 for two adhesive bands defined by $a_0^h = 0.025$ for the high adhesion zone and $a_0^l = 0.0025$ for the low adhesion zone.

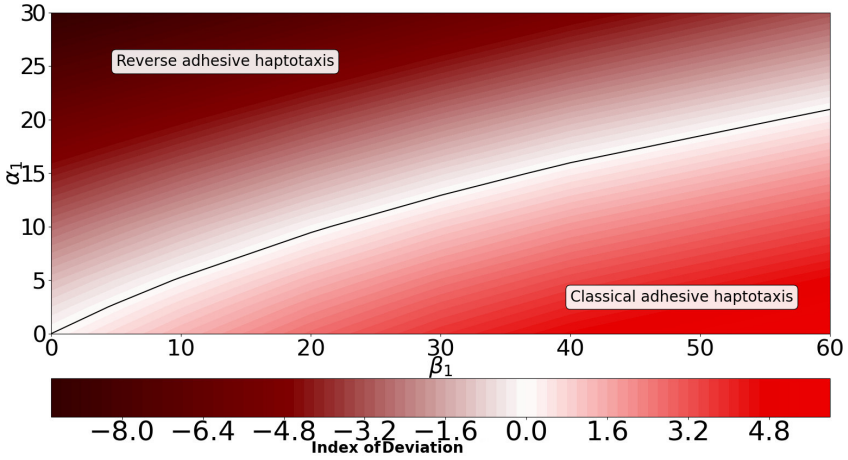

FIGURE B.3. Analogous to Figure 14 for two adhesive bands defined by $a_0^h = 0.025$ for the high adhesion zone and $a_0^l = 0.0025$ for the low adhesion zone.

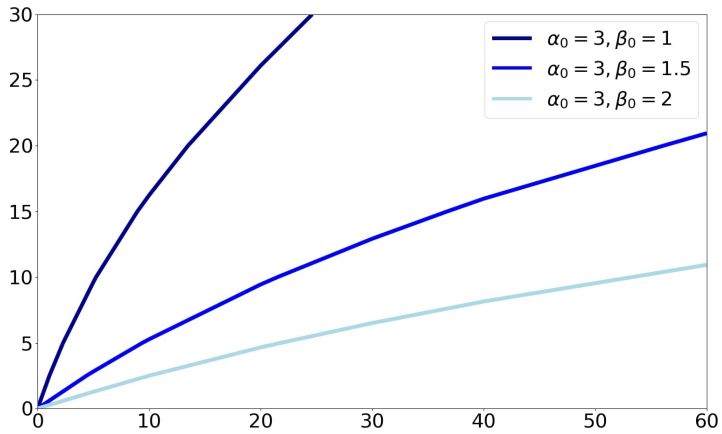

FIGURE B.4. Analogous to Figure 15 for two adhesive bands defined by $a_0^h = 0.025$ for the high adhesion zone and $a_1^l = 0.0025$ for the low adhesion zone.

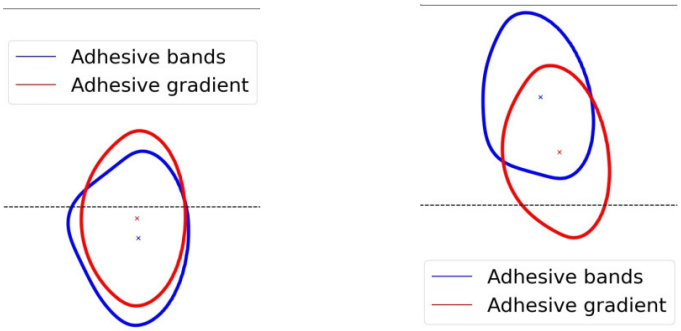

FIGURE B.5. Analogous to Figure A.1 and A.2 (right) at time $t = 65$ on an adhesion band and on an adhesion gradient between the values $a_0^h = 0.025$ and $a_0^l = 0$.

Finally, in Figure B.5 we see that varying a_0 in a gradient-like pattern maintain the correct qualitative behavior but slows down the effect as in Appendix A.